High resolution ambient noise tomography of the Southwestern Alps and the Ligurian margin

Gauthier Guerin, Diane Rivet, Anne Deschamps, Christophe Larroque, Aurélien Mordret, Jean-Xavier Dessa, Xavier Martin

Geophysical Journal International

Geophys. J. Int. (2020) **220,** 806–820
Advance Access publication 2019 October 21
GJI Seismology

doi: 10.1093/gji/ggz477

High resolution ambient noise tomography of the Southwestern Alps and the Ligurian margin

Gauthier Guerin,[1] Diane Rivet,[1] Anne Deschamps,[1] Christophe Larroque,[1] Aurélien Mordret,[2,3] Jean-Xavier Dessa[1] and Xavier Martin[1]

[1] *Université Côte d'Azur, CNRS, Observatoire de la Côte d'Azur, IRD, Géoazur, France. E-mail: gauthier.guerin@geoazur.unice.fr*
[2] *Department of Earth, Atmospheric and Planetary Science, MIT, Cambridge, MA 02139, USA*
[3] *Now at: Institut des Sciences de la Terre (ISTerre), Université Grenoble Alpes, CNRS, IRD, Gières, France*

Accepted 2019 October 18. Received 2019 September 6; in original form 2019 March 8

SUMMARY

The Southwestern Alps and the Ligurian margin is a region of moderate seismicity with a high rate of small to moderate events. Identifying the active faults in this very densely populated region is critical to better assess the hazard and mitigate the risk. An accurate 3-D velocity model of the shallow to middle crust is a fundamental step to better locate the seismicity, and hence, the faults from which it originates.

We performed ambient noise surface-wave tomography based on all available continuous seismological data from the French and Italian permanent networks (RESIF, INGV, RSNI), and current and past temporary experiments (AlpArray, CASSAT, SISVAR, RISVAL). In addition to these available data, we deployed three more stations to improve the spatial resolution in a region with sparse seismic station coverage. Overall, we used 55 inland seismic stations, 5 oceans bottom seismometers and 2 offshore cabled site/sensors. Data span the 2014–2018 time period. Time series from all available components were cross-correlated to reconstruct both Rayleigh and Love-wave Green's functions. For each station-pair Rayleigh and Love group velocity dispersion curves were semi-automatically picked using a frequency–time analysis. Then we regionalize these group velocities to build 2-D Rayleigh and Love velocity-maps between 1.5 and 9 s period. Using a two-step inversion, we estimate the best 3-D shear wave velocity model. The first step is based on a Neighbourhood Algorithm to recover the best three layers' velocity model at each cell of the model. We then use this three-layer model as a starting model in a perturbational method based on finite elements. At periods up to 5 s, the spatial variation of the velocity is well correlated with the effective geology of the area. Lower velocities are observed in areas where the sedimentary cover is thicker, such as the Var and Paillon valley near Nice, or in the subalpine domain in the northwestern part of the region. Higher velocities are retrieved in areas where massifs are present, such as the Argentera-Mercantour massifs in the northeastern, or the Esterel massif in the southwestern part of the region.

Key words: Europe; interferometry; Crustal imaging; Seismic noise; Seismic tomography.

1 INTRODUCTION

The Southwestern Alps-Ligurian basin junction is one the most seismically active zones of western Europe. It is presently an area of very low deformation rate and low- to moderate seismicity. Instrumental records display continuous microseismicity together with moderate-size events (M_L 3.5–5) and the horizontal velocity measured from 15 yr of continuous GPS is less than 0.5 mm yr^{-1} (Larroque *et al*. 2001; Nocquet 2012). Nevertheless, in 1887, a major earthquake occurred 20 km offshore Impera in the Ligurian sea (Larroque *et al*. 2012). It reached a macroseismic intensity of X (Medved-Sponheuer-Karnik scale) and an estimated magnitude of 6.7–6.9 (Ioualalen *et al*. 2014). This damaging earthquake occurred in a high vulnerability area, as more than 2 million people live on the French–Italian Riviera between Cannes and Genoa. However, the driving mechanism of such seismicity remains poorly understood (Béthoux *et al*. 1992, 2008; Larroque *et al*. 2009). A better understanding of the origin of the seismicity would contribute mitigating the risk. In this study, we provide a regional seismic velocity model of the Southwestern Alps-Ligurian basin junction that will be useful to better locate seismic events, and therefore to identify active structure which is a prerequisite to seismic hazard assessment.

1.1 Geological setting

The southwestern Alps is the result of a hundred million years of geological evolution dominated by the convergence between the Africa and Eurasia plates which led to the collision between continental blocks and to the building of the alpine mountain range from Cretaceous to Miocene times (Dercourt *et al*. 1986; Dewey *et al*. 1989). The southwestern French Alps are now made of the high elevation Argentera massif and the southern subalpine fold and thrust belts (Tricart 1984; Laurent *et al*. 2000) which are bounded on their western side by the Maures-Esterel Massif (Fig. 1). The Argentera and Maures-Esterel massifs are composed of crystalline rocks while the southern subalpine fold and thrust belts are composed of mesozoic and cenozoic sedimentary rocks. The emplacement of the Argentera massif and the southern subalpine fold and thrust belts is related to the late phase of the alpine orogeny (∼15–3 Ma, Riccou & Siddans 1986; Fry 1989; Bigot-Cormier *et al*. 2000; Sanchez *et al*. 2011) while the Maures-Esterel massif was mainly deformed during the hercynian orogeny and remains poorly deformed later.

During the convergence between the two plates, the Ligurian basin opened at Miocene times through this mountain range in response to the anticlockwise rotation of the Corsica-Sardinia block (Westphal *et al*. 1976; Gattacceca *et al*. 2007). The continental rifting started between 34 and 28 Ma and ended around 21 Ma (Réhault *et al*. 1984; Séranne 1999; Rollet *et al*. 2002). This was followed by a drifting phase between 21 and 16 Ma. The Ligurian basin is considered to be a backarc basin generated from the southeastward roll-back of the Apennines–Maghrebides subduction zone (Malinverno & Ryan 1986; Faccenna *et al*. 1997; Jolivet *et al*. 2008).

The studied area can then be divided between an onshore and an offshore domain and its complex geological evolution results in a heterogeneous crustal puzzle. At depth, the Moho is located ∼40–45 km below the high topography (up to 3200 m) of the Argentera and becomes shallower toward the south to reach a depth around 27 km below the coast (e.g. Masson *et al*. 1999; Thouvenot *et al*. 2007; Stehly *et al*. 2009; Schreiber *et al*. 2010). The northern ligurian margin is narrow and the continental crust thins abruptly in a few tens of kilometres from the coast and, in the basin, the oceanic crust is 4 km in thickness (Chamoot-Rooke *et al*. 1999; Rollet *et al*. 2002).

1.2 Ambient noise tomography

Ambient noise tomography is based on the reconstruction of the Green's function (GF) between different receivers from the cross correlation (CC) of long duration ambient noise records. In the 1–10 s period band, ambient noise tomography allows us to gain insight into the first tens of kilometres of the subsurface. Numerous ambient noise surface wave tomography has been performed at regional scale in densely instrumented areas (e.g. Lin *et al*. 2008; Stehly *et al*. 2009; Mordret *et al*. 2014; Giannopoulos *et al*. 2017; Schippkus *et al*. 2018). Regional seismic velocity models are important for seismic hazard assessment because they contribute to a better location of the seismic events and highlight the relationship between the seismicity and the crustal structures. Because surface wave tomography allows building a precise velocity model for the shallow and the middle crust, it also helps to better retrieve, on one hand, deeper discontinuities and structures in the deep crust and shallow mantle using body waves tomography (e.g. Rawlinson & Sambridge 2004; Nunn *et al*. 2014) and, on the other hand, serve as a reference model to study shallow structures (e.g. above 1 km depth) such as shallow sedimentary basin using geotechnics methods. The development of OBS with sufficiently long acquisition time, as well as the installation in some regions of permanent cabled OBS, allow imaging in the oceanic crust (e.g. Yao *et al*. 2011; Mordret *et al*. 2014; Hable *et al*. 2019).

Over the past 10 yr, the development of dense permanent seismic networks with high quality broad-band stations (RESIF-RLBP, GU, INGV) in the Southwestern alps—Ligurian allows to study the crustal structures with a high resolution. In addition to further increase the resolution we use continuous data recorded during current and past temporary experiments. This multiplication of deployed stations allows us to break away from the uneven spatio-temporal distribution of seismicity using the ambient noise tomography.

At the scale of the whole Alpine continental collision zone, Verbeke *et al*. (2012), Molinari *et al*. (2015), Kästle *et al*. (2018) and Lu *et al*. (2018) recently performed ambient noise tomography to image the velocity structure from the middle crust to the upper mantle and the Moho depth. These previous works did not used OBS and were investigating surface waves with long enough periods so that the water layer could be neglected since Scholte waves can be regarded as Rayleigh waves. The originality of this present work is to take advantage of an amphibious seismic network at a regional scale to image both the continental crust and the continental margin.

Here, we present the tomography of Southwestern Alps/Ligurian Sea by using Rayleigh, Scholte and Love waves altogether. First, we estimate Rayleigh, Scholte and Love wave group velocity maps from the dispersion curves of ambient noise cross-correlation. We then invert for the shear velocity at depth from the regionalized Rayleigh and Scholte wave group velocities.

2 CONTINUOUS SEISMOLOGICAL DATA

We

À used continuous seismic ambient noise records of short-period and broad-band sensors of the French [RESIF (1995)–28 stations] and Italian [INGV Seismological Data Centre (1997)–8 stations, Regional Seismic Network of Italy–6 stations] permanent seismic networks as well as 18 temporary stations set up for past or current experiments [AlpArray Seismic Network (2015)—Hetenyi *et al*. (2018)], POSA (French National Research Agency ANR), CASSAT, SISVAR and RISVAL (European Alcotra programs). In addition, data from 5 ocean bottom seismometer from AlpArray-Ligure program deployed during 2 months in 2017 and 2 off-shore cabled seismometer from European EMSO-Ligure program have been used to image the French part of the Ligurian Sea. Finally, we installed three temporary stations during 3 months in order to increase the resolution in the western part of our velocity model where the permanent stations coverage is less dense. Overall, we used continuous seismic noise of 62 stations across the Southern Alps and the Ligurian Sea between 2011 and 2018, which allows us to exploit 1411 and 970 station pairs for the vertical–vertical and transverse–transverse components, respectively. In this study, the seismic record range goes from 3 months up to 1 yr in length. Among these stations, 12 are single-component stations. The interstation distances range from 500 m in the Var valley to 250 km between Italy and France. Fig. 2 shows an overview of the study area and the locations of the stations.

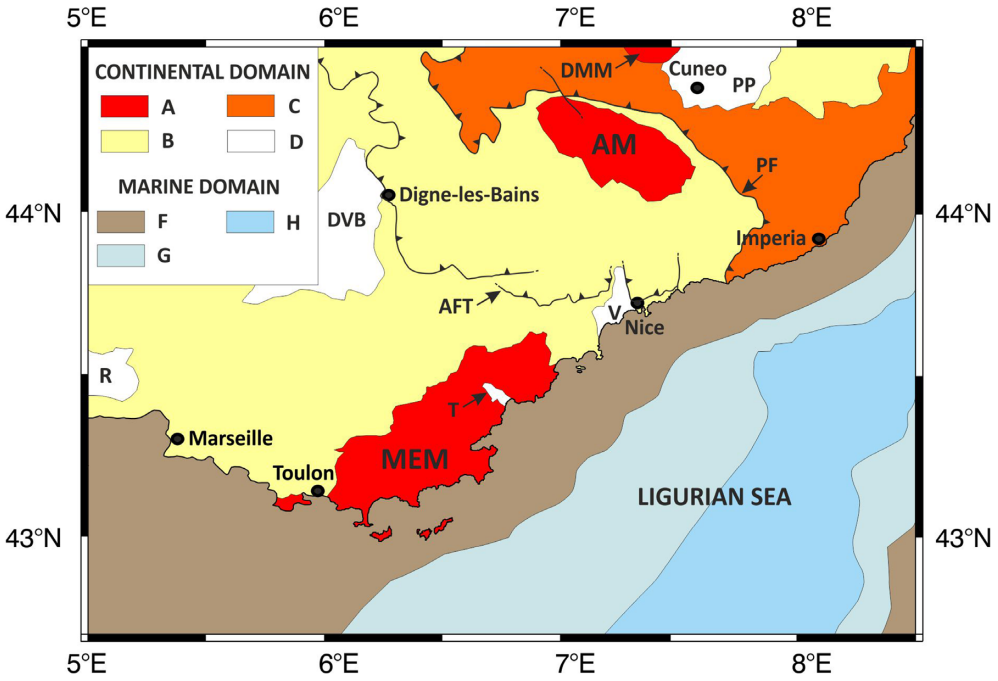

Figure 1. Simplified geological map of the Southwestern Alps—Ligurian sea area (from Carte Géologique de France, BRGM and Rollet *et al*. 2002). Continental domain: A, Palaeozoic crystalline basement (AM: Argentera Massif, DMM: Dora Maira Massif, MEM: Maures-Esterel Massif); B, Meso-Cenozoic sedimentary cover of the external alpine belt; C, sedimentary cover of the internal alpine belt; D, Plio-Quaternary sedimentary deposits (DVB, Durance-Valensole basin; PP, Po Plain; V, Var basin; R, Rhone basin; T, Tanneron basin); AFT, Alpine frontal thrust; PF, Penninic front (internal alpine thrust). Marine domain: F, thinned continental crust of the Ligurian margin; G, transitional oceanic–continental crust; H, oceanic crust.

3 AMBIENT NOISE SURFACE-WAVE TOMOGRAPHY

3.1 Seismic noise cross-correlation

We performed the ambient noise tomography of the Southwestern Alps following the approach developed by Stehly *et al*. (2009) and Mordret *et al*. (2014). The first step consisted in retrieving empirical GF between all station pairs from CCs of ambient seismic noise and measuring the frequency-dependent group traveltimes from every station pair CC. Then, we built 2-D group velocity maps at each period by inverting the surface wave traveltimes. Finally, we inverted both Rayleigh and Love-wave group velocity maps, with the aim of deriving the structure at depth inverting dispersion curves for a 1-D shear-velocity model in every cell of the grid. The latter was performed by using two different methods described afterwards. One of specific features to take account for depth inversion is that ambient noise at the seafloor is composed of Scholte waves which are surface waves found at interface between rock basement and sea. The presence of a water layer in a model makes the guided Scholte waves slower at the same frequency compared with the Rayleigh waves.

3.2 Pre-process and cross-correlation computation

In order to obtain the most stable GF, a pre-processing was applied on all raw data following Bensen *et al*. (2007). The first step consists in removing the mean and the trend of the signal, bandpass filtering between 0.02 and 2.5 Hz, decimating the signal to 5 Hz, and removing the instrument response. The second step aims at removing glitches and earthquakes by clipping amplitudes greater than 10 times the standard deviation estimated daily. Then a spectral whitening between 0.02 and 2.5 Hz was applied before removing part of the signal with amplitudes greater than three times the standard deviation. Finally, a one-bit normalization was applied. This procedure is common for that type of study and applied to all single day of continuous seismic recordings.

From the pre-processed daily time-series, we computed all the cross-correlations for Z, N and E components for each station pair (ZZ, NN, EE, EN and NE). We rotate the cross-correlation tensor to retrieve radial–radial (RR), radial–transverse (RT), transverse–radial (TR) and transverse–transverse (TT) components to recover both Rayleigh and Love waves (Lin *et al*. 2008). The ZZ, RR, ZR and RZ components of the cross-correlations are used to estimate Rayleigh waves velocity, while the TT component is used to estimate Love waves velocity. However, in order to estimate Rayleigh waves velocity only the ZZ component of the cross-correlations are used because it has a significantly higher signal-to-noise ratio (SNR) than RR, ZR and ZR counterparts.

To improve SNR, we finally stacked all daily cross-correlations for all available periods and merged the two-sided signal into a one-sided one by averaging positive and negative lag times. Most of the CCs with SNRs greater than 1.5 are found for station pairs located between 10 and 80 km apart.

3.3 Dispersion measurement

After getting the estimated GF from each station pair, we can retrieve group velocities of surface waves by using traditional frequency–time analyses (FTAN, Levshin *et al*. 1989). Given the number of CCs extracted (more than 3000), group velocity dispersion curves are commonly picked automatically. However, dispersion curves having a low SNR due to high-amplitude surface wave overtones or scattered waves in the signal are picked manually, thanks to a

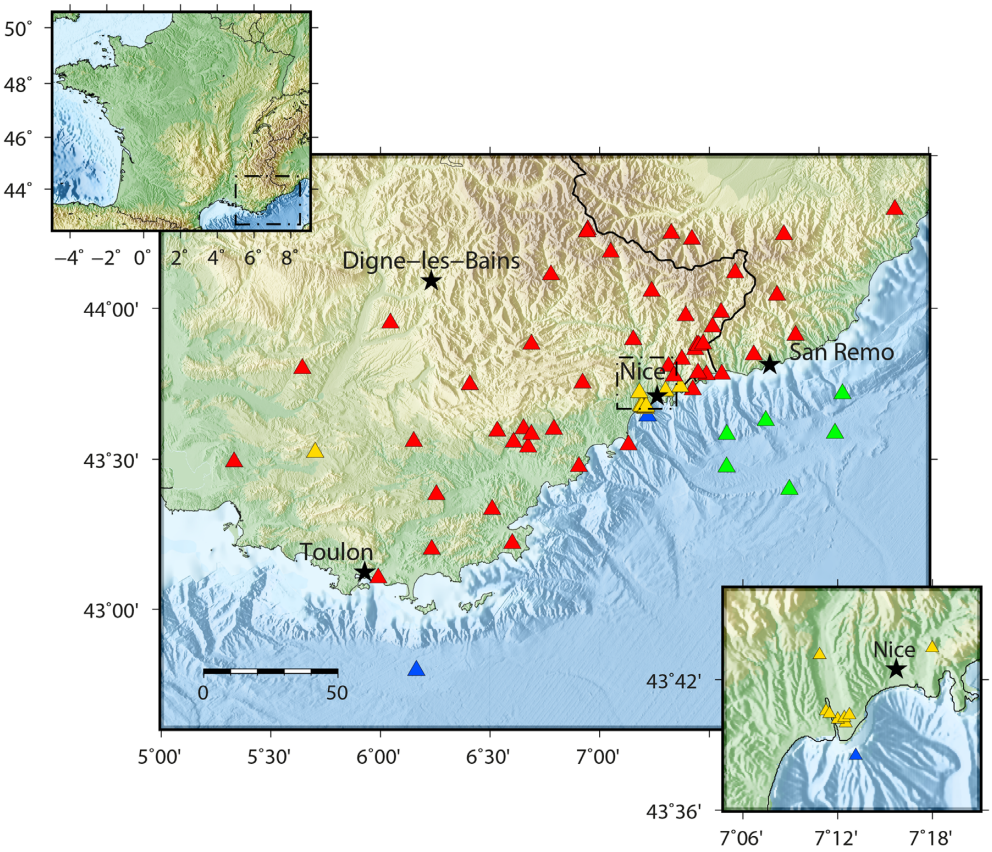

Figure 2. Map view of the southwestern Alps and the Ligurian margin with the location of the 62 stations used in this study. Red triangles correspond to broadband stations, yellow ones correspond to short-period stations, green ones correspond to OBS and blue ones correspond to permanent cabled OBS. The black stars indicate the main city. The region shows a high topography gradient from –2500 m in the Ligurian basin to 3300 m in the Argentera-Mercantour Massif distant of 70 km.

Graphical Users Interface developed by Mordret *et al*. (2015). It allowed us to select the best dispersion curves and mitigate above-mentioned effects. We used both Love and Rayleigh waves to see if there are structures affected by significant radial anisotropy in this area, revealed by strong differences between the horizontal and vertical shear velocities. Fig. 3 presents the Rayleigh wave extracted from the cross-correlation between A206A-LEPF and the dispersion of the group velocity, with phase velocity increasing with period.

Fig. 4(a) shows the cross-correlation surface waves on which the picking has been done to retrieve group-velocity as a function of periods. Fig. 4(b) shows period-velocity diagrams for the station pair A206A-LEPF (80 km interstation distance) for the three ZZ, RR and TT components. The frequency–time diagrams use the dispersion of the surface wave to obtain group-velocity measurements. The black dots correspond to the relative maxima of the diagrams whereas the white circles show the manually validated maxima corresponding to the fundamental mode. The latter are interpolated and smoothed by a fifth-order polynomial represented by the black curve.

We noticed that ZZ and RR component dispersion curve are picked in the same periods range and exhibit almost similar speed. On the other hand, the TT dispersion curve seems to show velocity faster than for the Rayleigh's wave component. Because many stations were temporary stations the RR components got the least amount of energy and have a lower SNR. Therefore, in the following we consider only the ZZ dispersion curve to invert of the Rayleigh wave group velocity map.

The number of dispersion curves picked as a function of periods for ZZ and TT components is presented in Fig. 5(a). The error bars present the standard deviation of the mean dispersion (red curve) from 1.5 to 9 s. For the same reasons that RR component (low SNR), we picked less TT component dispersion curve number than ZZ. Overall, we noticed that our ZZ and RR components seems to have similar lowest speed, as compared to TT components (Fig. 5a). We can observe that most of the dispersion curves are in range from 2 to 8 s periods with a deterioration of quality above 9 s and below 2 s. The number of available paths for periods greater than 9 s is not sufficient to be exploited further for the group velocity maps. Imaging deeper structures, as recently done by Kästle *et al*. (2018) and Lu *et al*. (2018), using longer periods waves, would have implied adding more distant stations, and is out of scope of this current work. We retrieve a total of 1172 (83 per cent) of usable traveltime measurements from ZZ component and 781 (80 per cent) from TT, each of them having a different period range. A summary is presented on the Fig. 5.

3.4 Rayleigh-wave group velocity maps

Group velocity maps are generated using the method of Barmin *et al*. (2001) which is based on ray theory involving a regularization

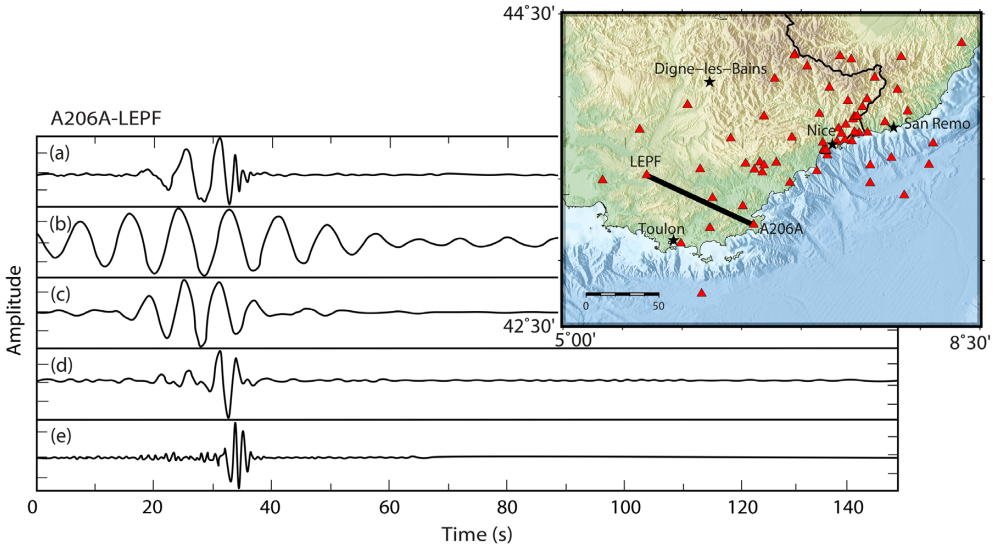

Figure 3. Cross-correlation between A206A-LEPF filtered for several labelled period bands and computed for the ZZ components of ambient noise. (a) Broad-band signal (0.4–14 s passband), while filtered signal is shown below with (b) 8–10 s, (c) 5–8 s, (d) 2–5 s and (e) 0.4–2 s. Black curve on the map indicates the path A206A-LEPF. Inter tations distance is 80 km.

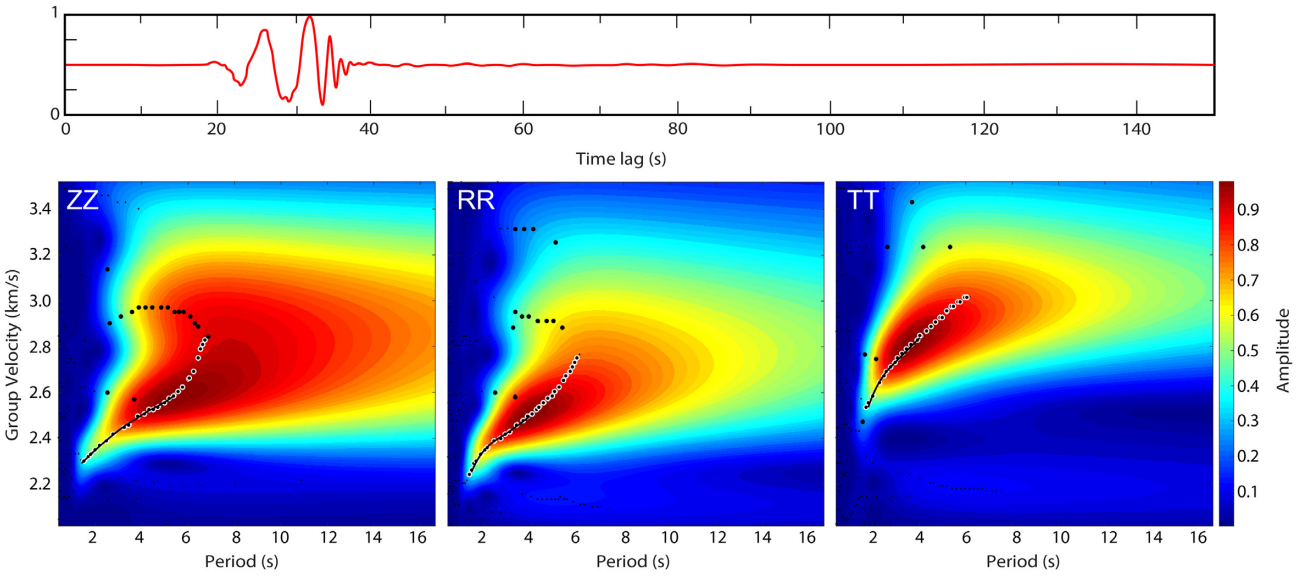

Figure 4. (a) Cross-correlation between A206A-LEPF pair station for ZZ component. Red signal represents the correlation. (b) Example of dispersion curve picking on the frequency–time for all three-components ZZ, RR and TT. Warm colours showing the maxima of energy in the signal. Black dots represent the relative maxima of the diagram for the instantaneous frequency. White circles highlight the automatic picking of these points. The black line is a five-order polynomial fitting to the automatic picks.

function. This function is composed of a spatial Gaussian smoothing function and a constraint on the amplitude of the perturbation depending on local path density. We used a Cartesian version of this algorithm which is described by Mordret *et al.* (2013). We performed two successive inversions to regionalize surface wave group velocities over a 22 × 38 grid, with a cell size of 9.42 km x 9.42 km. The initial model has a constant velocity equal to the mean group velocity for each period. The first inversion computes an overdamped model with all paths to remove outliers. For this purpose, we discard all paths for which the difference between the measured traveltime (Fig. 6) and the traveltime computed during the first inversion is greater than twice the standard deviation. Overall, they represent less than 5 per cent of the selected paths. The second inversion is performed with the optimal smoothing and damping parameters. The cells of the model with less than 4 rays are discarded.

We inverted both measured Rayleigh and Love wave dispersion curves group velocity map at 16 periods with a step of 0.5 s between 1.5 and 9 s. We do not take into account the topography during the inversion procedure. Most of our interstation paths with large topographic contrast correspond to long distances with mostly sensitivity at long periods. As shown in Köhler *et al.* (2012), the

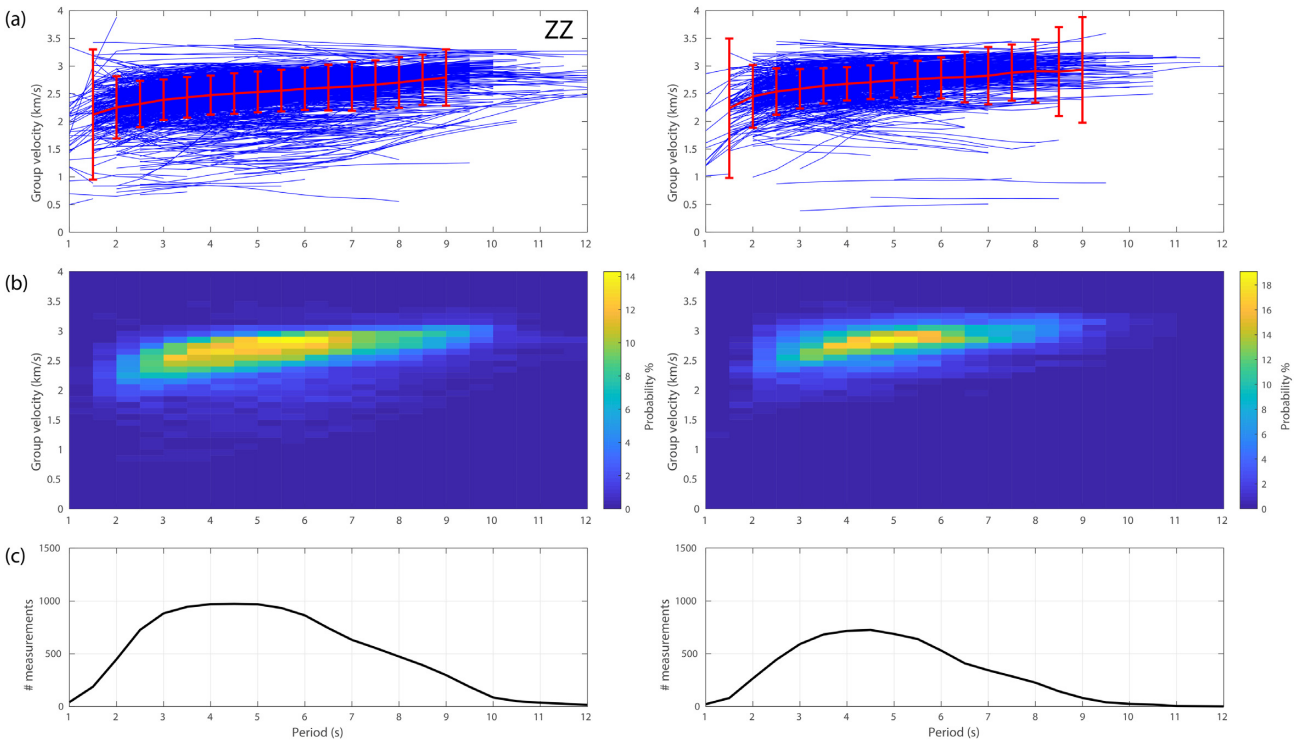

Figure 5. (a) All measured Rayleigh and Love-wave dispersion curves are plotted on a group velocity-period diagram. The average dispersion curve with its standard deviation is plotted as red line and only for periods ranging from 1.5 to 9 s which are the periods shown on group velocity maps (b) Probability density diagram of the dispersion curves. (c) Diagram representing the number of measurements with respect to period for ZZ (left-hand panel) and TT (right-hand panel).

topography effect at long distances, is averaged out by 3-D effect, and its impact on wave velocity measurements is negligible.

We present our final group velocity maps for both Rayleigh and Love waves group velocity at range periods from 1.5 to 9 s with a step of 0.5 s (resp. Figs 7 and 8). The mean variance reduction of the traveltime residual shows values around 50 per cent indicating that those velocities models fit well. If we compare group velocity map at each period for the ZZ and TT components, we can notice that Love wave velocity is on average higher for all identified structures.

On both Rayleigh and Love group velocity maps, we observe two high-velocity anomalies in the northeastern and southwestern part corresponding, respectively to the Mercantour Argentera Massif—Briançonnais zone and the Esterel-Maure massif. We identify a low velocity anomaly area around Nice and overall on the coastline. A localized low velocity anomaly centred on the Var Valley (V on Fig. 1) is clearly observed on the Love group velocity map up to 4 s. A large low velocity anomaly zone is observed up to 8 s on the northwestern part of both the Rayleigh and Love group velocity maps, spatially correlated with a Subalpine thrust mass with Cretaceous and Jurassic carbonates, with lowest velocity centred on the Valensole plio-quaternaire bassin (VSB). Lastly, on the Rayleigh–Scholte group velocity maps the lowest velocity anomaly is observed in the Liguria sea for each available period. This low velocity zone arises from the slower velocity of the Scholte waves, which are very sensitive to the *P*-wave velocity of the sea water layer for the periods band of interest.

3.5 Resolution

It is essential to assess the spatial resolution of each group-velocity maps to estimate their geometrical accuracy. In our main study area (the southern termination of the Alps), where station coverage is very dense, we got on average more than 80 paths per cell. In this case, the resolution length is expected to tend towards the model's cell size. In the western, and easternmost areas, the low station density as well as the fact that the majority of paths exhibit large interstation distances (lowest SNR at 4 s) yields an expected loss in spatial resolution.

Fig. 9(a) shows the average resolution at 4 s, estimated from the resolution matrices (Barmin *et al*. 2001; Mordret *et al*. 2013). The resolution matrix is the response of the tomographic process to a Delta function type anomaly located in a corresponding cell of the model. It indicates how accurately the tomography is able to retrieve the anomaly. Overall, in our 2–9 s period band, the resolution of the group velocity map is good with a maximum of 35 km wavelength at the limit of our study area. From the Var to the Italian border, where ray coverage is dense, the spatial resolution decreases to around 10 km wavelength. Fig. 9(b) represents the resolution shift which is the actual position of the spot with respect to its theoretical position and it shows if the observed anomalies are at the right position on the map. Nearly all the shift resolution is ranging between 0 and 5 km, which means that the retrieved anomalies are located in the correct cell.

3.6 Shear-velocity inversion

Rayleigh and Love-wave group velocity maps provide information about lateral variations of surface wave velocities with respect to the period. In order to obtain insight into the structure at depth, we extract all available local regionalized dispersion curves to construct a local 1-D shear velocity model. Then, we combine all those 1-D profiles from all cells to construct the final 3-D shear velocity

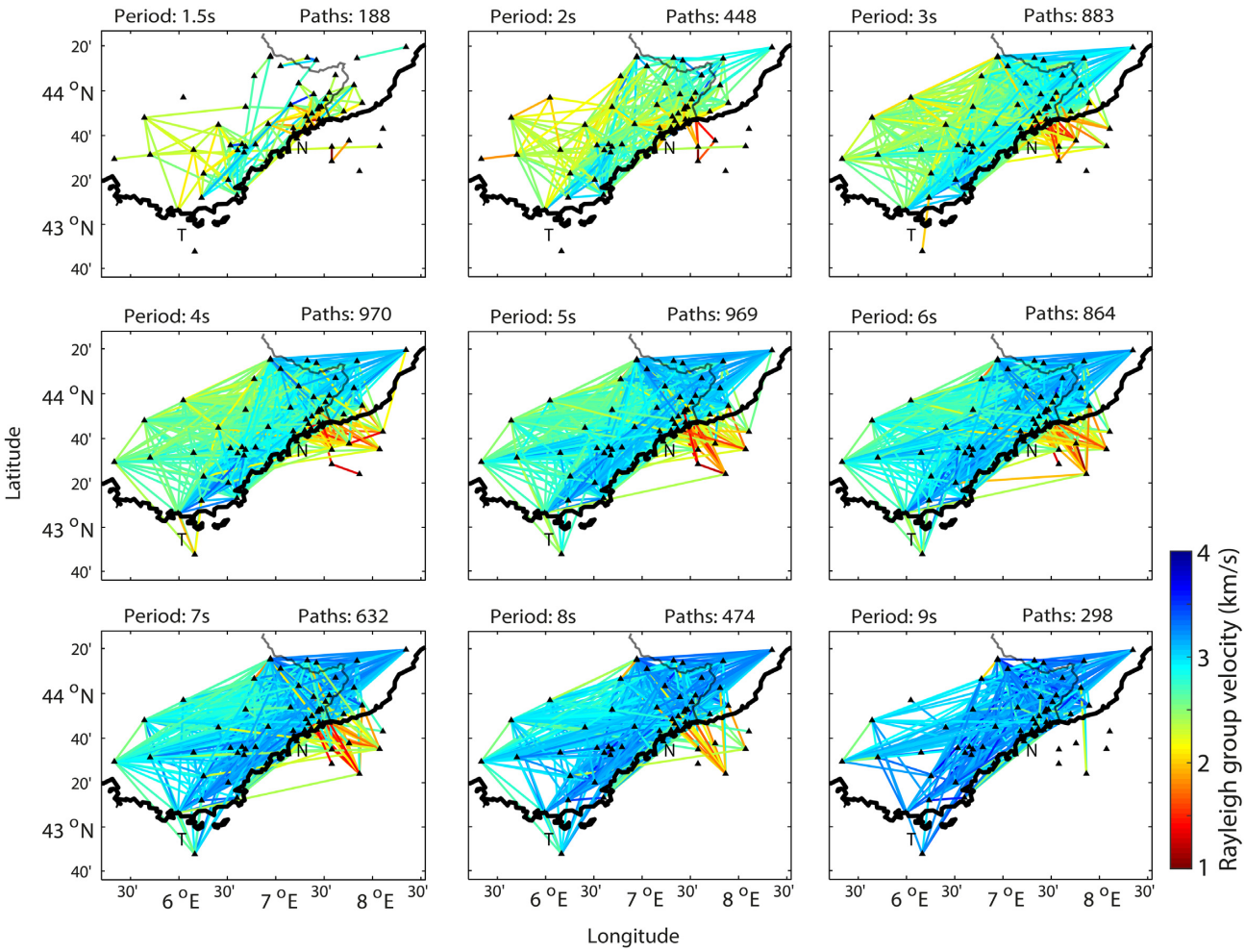

Figure 6. Rayleigh-wave group velocity measurements for ZZ components and associated ray path coverage to periods from 1.5 to 9 s. Seismic stations are shown as black triangles. T indicates the city of Toulon. N indicates the city of Nice. Grey curve shows the Franco-Italian border.

model. As a reminder, we used a 22 × 38 grid with a cell size of 9.42 km x 9.42 km.

3.6.1 First inversion: The Neighbourhood Algorithm

As mentioned previously, we performed a two-step inversion. The first inversion is based on the Neighbourhood Algorithm, an optimized Monte Carlo global search technique developed by Sambridge (1999a, b) to sample a model-space, which has been efficiently deployed in different geophysics inversions (e.g. Mordret *et al*. 2014, 2015; Giannopoulos *et al*. 2017). A model is a set of different parameters and the corresponding model-space is a multi-dimensional space having the same dimensions as the number of the parameters used to characterize the model. For each parameter of our model-space, we fixed an *a priori* range of value. Hence, for our local dispersion curve inversion problem, the model is a 1-D layered shear-wave velocity profile with two parameters for each layer, the thickness and the *S*-wave velocity. For the two following inversions, we take in account that ambient noise at the ocean floor is composed of Scholte wave and therefore add an extra water layer for offshore cells. We used SHOM MNT bathymetry (Shom 2015) to estimate the mean depth, ranging from 1800 to 2200 m, for of each off-shore cell. More information about the methodology features in Mordret *et al*. (2014).

All our local 1-D shear velocity model are based on an initial model with three layers over a half-space with five unknowns: three *S*-wave velocities and the depths of two interfaces separating them. More than 27 000 models have been sampled for each cell during this inversion. Figs 10(a)–(c) shows the 1-D dispersion curves with the red errors bars derived from the initial measured dispersion curves, and on which the depth inversion is computed. We average the 100 best models to get the final model which corresponds to the red curves in Figs 10(d)–(f). The other colours curve indicates all the models sampled. The misfit between the measured and the theoretical dispersion curves is the area between the theoretical curve and the uncertainties of the observed dispersion curve normalized by the area inside the uncertainties of the measured dispersion curves as defined in Mordret *et al*. (2014). The misfit of the best model is on average lower than 0.01. This three-layer depth inversion allows to identify major features of the studied region. As an example, we computed three models which have specific *S*-wave velocity anomalies. Figs 9(a) and (c) show high anomalies that correspond, respectively, to the crystalline Mercantour-Argentera massif and a part of the Maures massif and Fig. 9(b) shows a lowest velocity anomalies zone around Nice and the Var valley with thick sediment deposits. We can notice two similar patterns corresponding to the Argentera-Mercantour (Fig. 10d) and the Maures massif (Fig. 10f), with a first layer exhibiting a shear-wave velocity of ∼2.4 km s^{-1} at

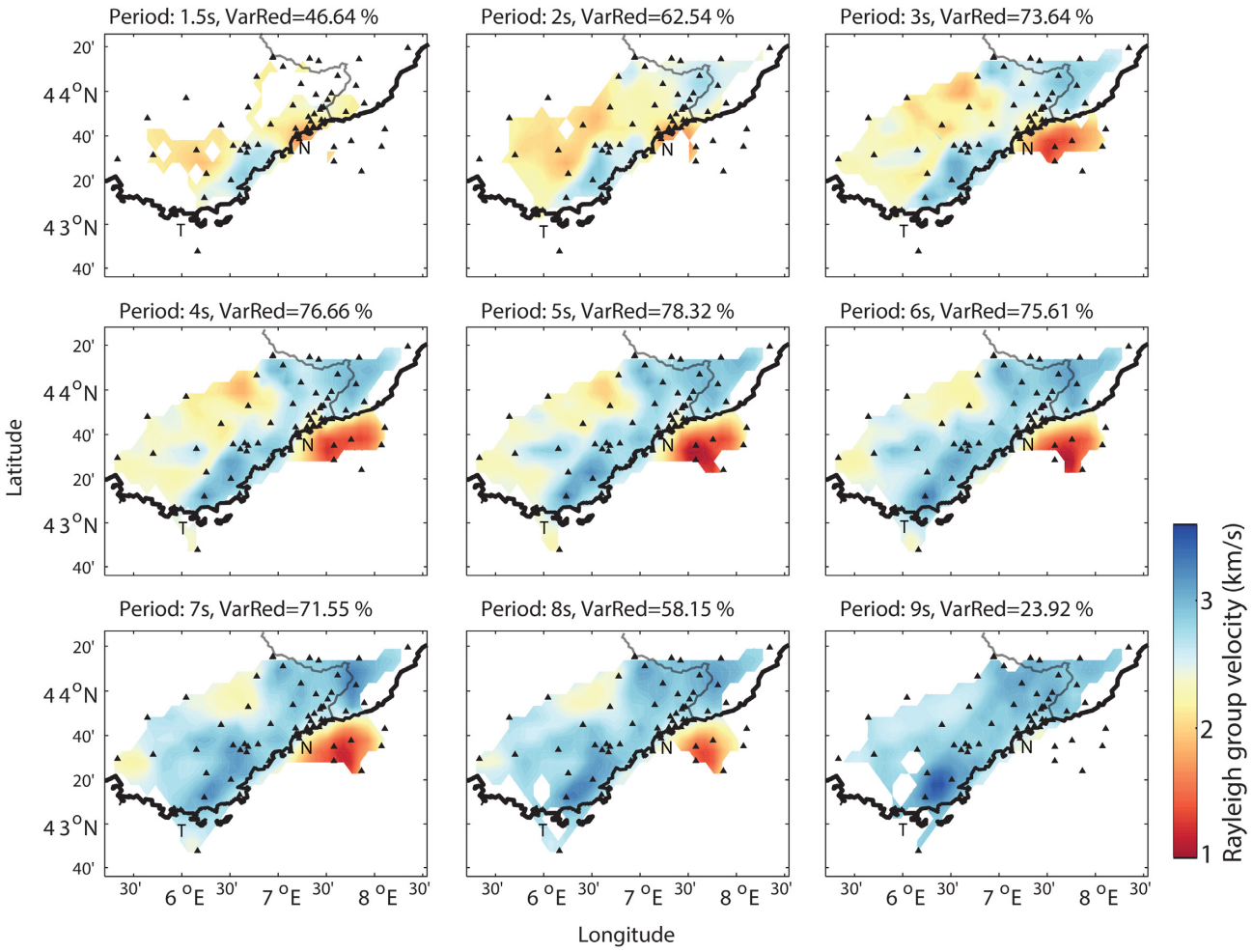

Figure 7. Rayleigh and Scholte wave group-velocity maps for 1.5, 2, 3, 4, 5, 6, 7, 8 and 9 s, respectively. At each period, we indicated the variance reduction (VarRed) between data computed from the measurement and the final model. The black bold curve shows the coastline while the grey curve indicates the Franco–Italian border. Seismic stations are shown as black triangles. T indicates the city of Toulon. N indicates the city of Nice.

2 km depth, a second layer up to 5–7 km depth with ∼2.8 km s^{-1} velocity and lastly, a ∼3.4 km s^{-1} velocity found in the third layer. From the known geology of the area, we can assume that the sedimentary cover lies between the surface and the first layer, then a second layer corresponding to the crystalline substratum. When looking at the second location (Fig. 10b) corresponding to an area between Monaco, Nice and the Var Valley, we can see a first 1 km deep layer of ∼1.9 km s^{-1} *S*-wave velocity underlined by a second one with a mean velocity of ∼2.1 km s^{-1} down to 3 km depth. Given the number of stations in this area, a good part of the short period (<2 s) were picked and therefore we have a better resolution to image the shallow crust.

3.6.2 Second inversion: perturbational inversion

We then perform a second inversion based on a perturbational method using finite elements (Haney & Tsai 2017). The individual finite elements, or layers, must be thin compared with the wavelength to ensure accuracy. Here, the frequency is fixed while the wavenumber and material properties are perturbed. It yields a first-order result relating perturbations in phase/group velocity to perturbations in the material properties.

This second inversion allows to refine the depth-dependent *Vs* profiles with a finer depth discretization of the models. As inputs, we use the three-layer model generated previously as well as the 1-D dispersion curves. Those three-layer models are smoothed prior to the perturbational inversion by applying a linear interpolation.

Here, a multilayer parametrization with different thicknesses is considered, instead of merely three layers. It exists an optimal depth discretization with an increasing thickness in depth. Such layering allows us to properly sample the Rayleigh waves at any depths. This optimal layering for Rayleigh-wave modeling is based on a phase velocity dispersion curve. Following Haney & Tsai (2017), we find that our optimal number of layers is around 40 on land, and 30 at sea. The water layer is discretized into 10 layers with varying thickness to reach a depth ranging from 1800 to 2200 m. The total depth of the model is 30 km, allowing to recover good accuracy in the first 10 km depth. As 2 smoothing factors, we set the smoothness scale at 3 km (half-space depth), and the model standard deviation factor at 4 for every cell. Considering the sensitivity depth of the Rayleigh Wave with periods, most of the layers are sampled in the upper third of the model. In Fig. 11(a) shows an example of dispersion curves on which models are generated for a cell located below Nice. Given that the first inversion misfit is good, we decided to lower the velocity values errors by a factor 2 (black error

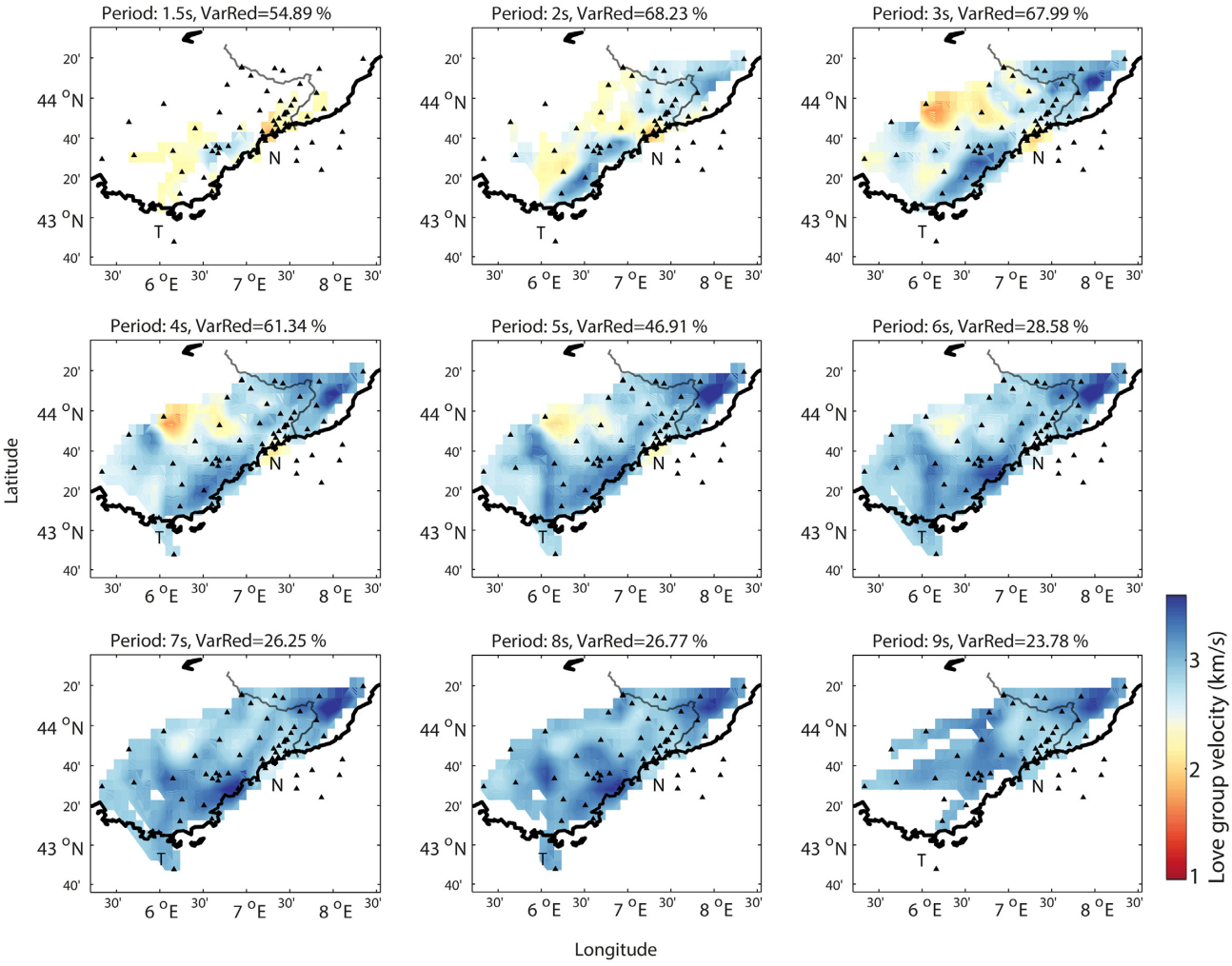

Figure 8. Same as Fig. 7 but for Love wave group-velocity maps for 1.5, 2, 3, 4, 5, 6, 7, 8 and 9 s, respectively.

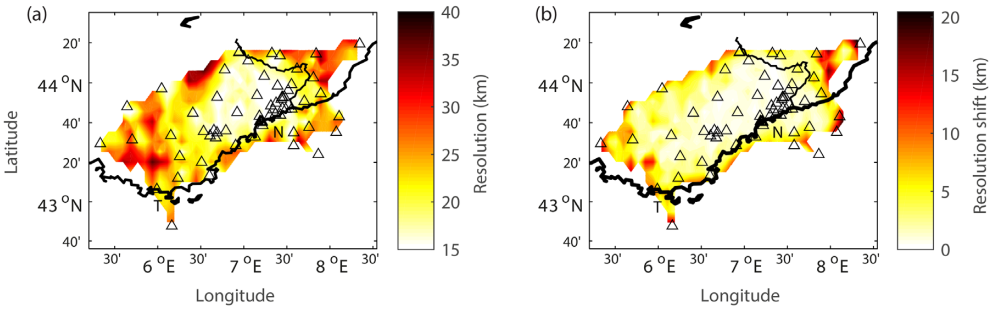

Figure 9. (a) Spatial resolution map for Rayleigh waves at 4 s. (b) Resolution shift map for Rayleigh wave at 4 s. For the two figures, the black bold curve shows the coastline. Seismic stations are shown as black outline triangles. The black bold curve shows the coastline. The thinner black curve indicates the Franco–Italian border.

bars in Fig. 11a). We noted that the second inversion improved the misfit, especially at low frequencies. The final update (red curve) predicts overall more than 95 per cent of the group velocity measurements. We generated the models with a chi-squared value below 1. Fig. 11(b) shows the corresponding three-layer (green curve) and multilayers (red curve) models resulting from our successive inversions.

The final step consists in collecting the best-fitting 1-D depth profiles for each grid cell and in generating a 3-D shear-velocity model of the southwestern Alps and Ligurian margin. In Fig. 12, we present selected depth (600, 2000, 3800 and 6400 m) slices of our final 3-D shear-velocity model.

Fig. 13 shows a slice at 300 m depth zoomed in the Alpes-Maritimes district and the city of Nice. In this area, the density

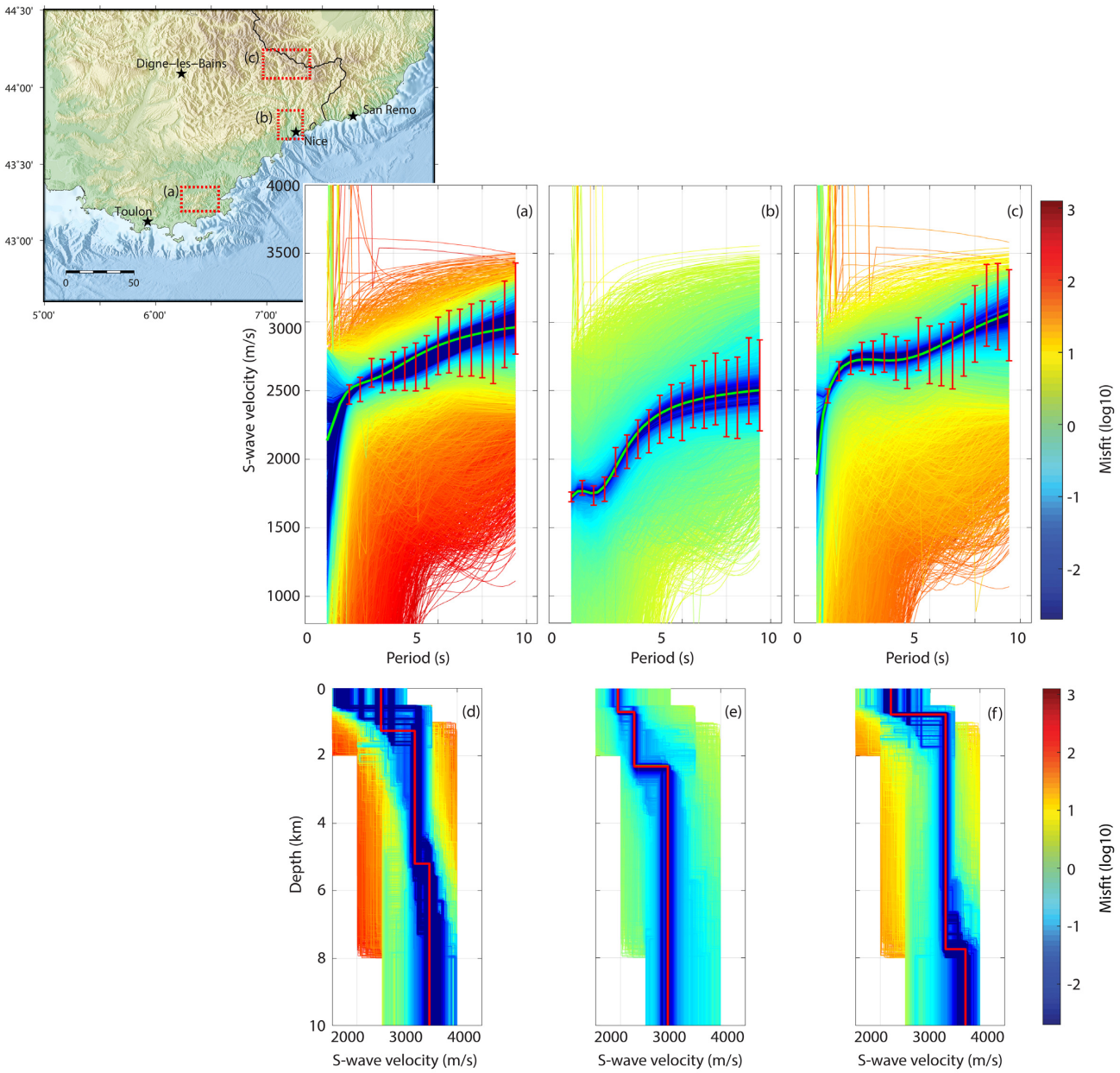

Figure 10. Inverted shear wave velocity model for specific locations in our study area: (a) and (d) feature the Mercantour-Argentera massif (rectangle a in the inset map); (b) and (e) an area around the Var (rectangle b in the inset map); (c) and (f) is the eastern part of the Maures massif (rectangle c in the inset map). (a), (b), (c) show in red the error bars of the regionalized 1-D Rayleigh waves dispersion curves from which the shear wave inverted models are computed, in colour-coded the computed Rayleigh waves dispersion curves with respective misfit, and the green lines featuring the models with minimum misfit. (d), (e), (f) shows the associated inverted models with colour-coded misfit, the red lines representing the best-fitting model. Our final model is taken as the average of the 100 best models, with the lower misfit.

of stations provides a quite sufficient resolution to allow retrieving velocities which correlate with local geology. The low velocity anomaly surrounding Nice arises from the sedimentary basin of the Var and Paillon rivers on its western part and from the presence of weak marl and calcareous-marl of cretaceous and ologicene–pliocene ages, with an overall thickness reaching approximately 700 m (Jourdon *et al*. 2014), on its eastern part.

In Fig. 14, we show three 2-D profiles highlighting the main structures in the area. Profile P3 (west–east section) is aligned along the coast from the Maures massif to the Ligurian sea. Profiles P1 and P2 (north–south sections) highlight topography between inland massifs and the margin/basin system.

4 INTERPRETATION AND DISCUSSION

Although recent surface wave tomography studies covering the southwestern Alps were performed using the dense and large Alparray network, they cover the whole Alpine continental collision zone to obtain information in the crust and the upper mantle (Kästle *et al*. 2018; Lu *et al*. 2018). In this study, we opted to focus on the shallow crust, down to 10 km depth, where most of the seismicity is occurring in the region. Hence, a first comparison can be done on the Rayleigh and Love group velocity map at 8 s with the larger scale Alpine tomography. We found Rayleigh wave group velocity to be above 2.8 km s^{-1} on average and Love wave velocity group above

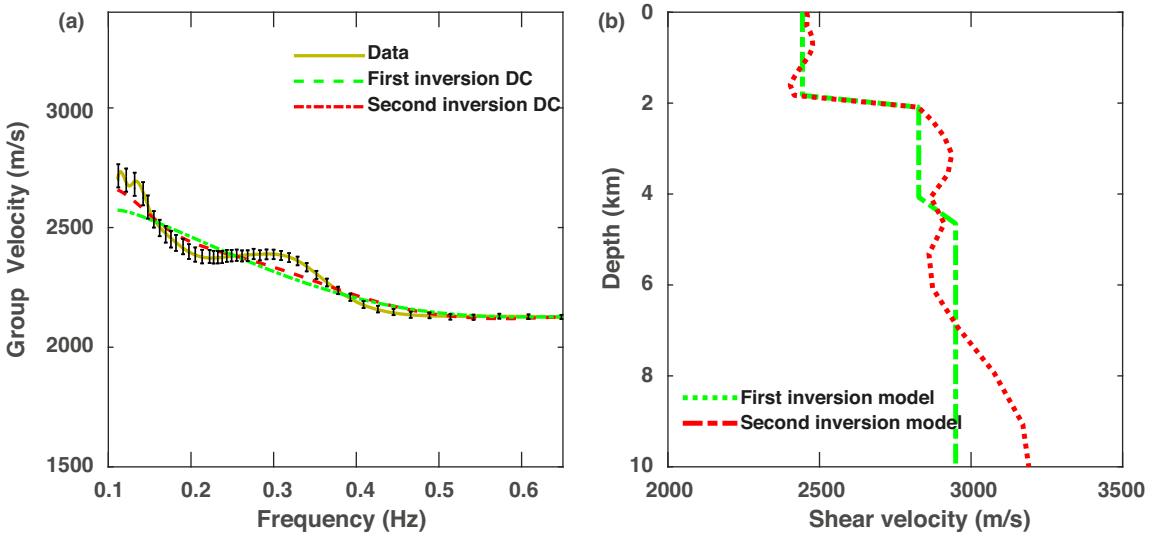

Figure 11. (a) Group velocity dispersion curves for the cell below the city of Nice: data from dispersion measurement (yellow), synthetic DC from the three-layer model (green), and from the multilayer model (red). (b) Shear velocity depth models using group velocities: initial three-layer model (green) and final multilayer model (red). The black error bar is computed the same way as the first inversion but divided by a factor of 2. chi-squared is less than 0.5 for this cell.

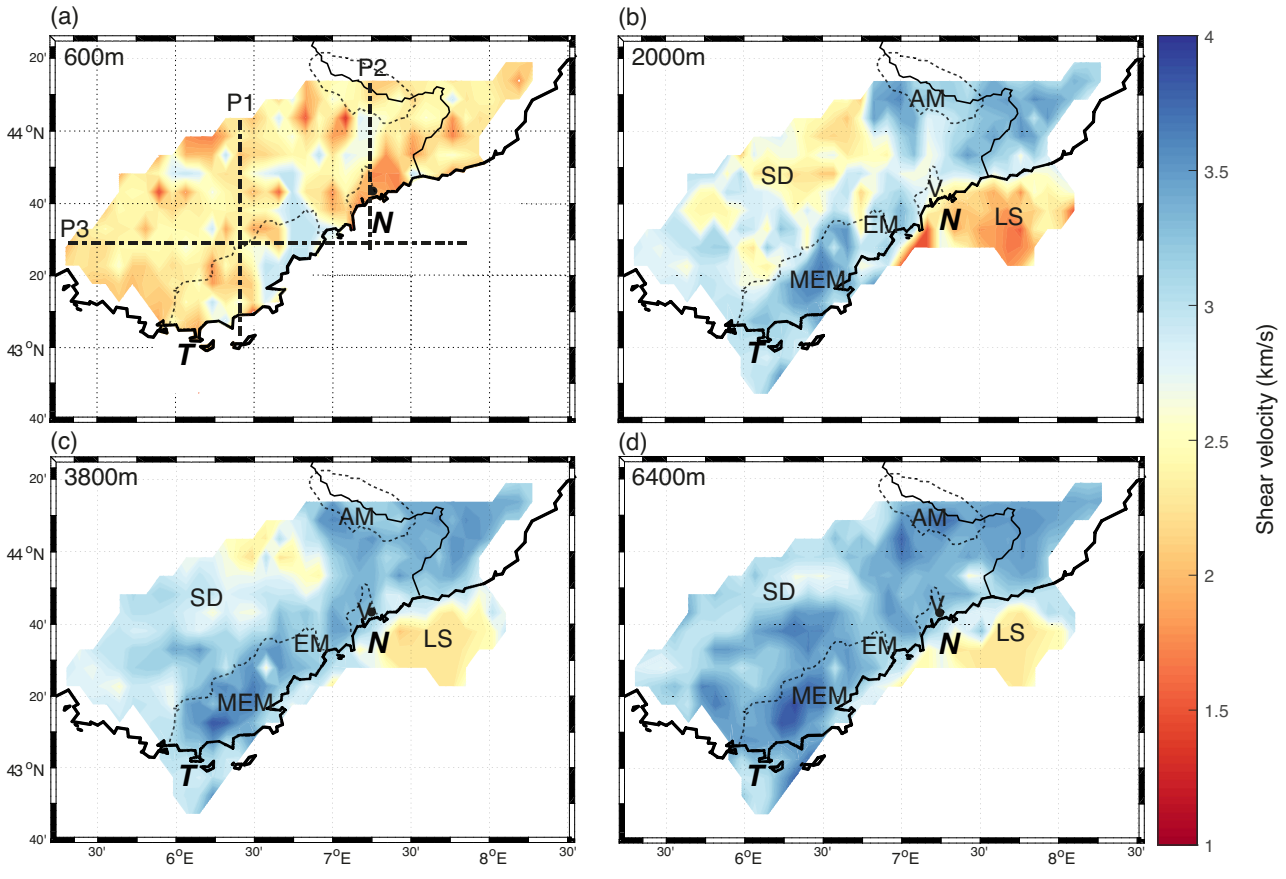

Figure 12. Depth slices through the 3-D final shear-velocity models at (a) 600 m, (b) 2000 m, (c) 3800 m and (d) 6400 m below the sea level. Major toponyms and areas are labelled: T, Toulon; N, Nice; V, Var and Paillon basin; SD, Subalpine Domain; AM, Argentera Massif; MEM, Maures-Esterel Massif; EM, Esterel Massif; LS, Ligurian Margin. The dashed lines in (a) represent the surface trace of extracted 2-D profiles shown in Fig. 14. The lowering opacity black curves feature the main structures in the region.

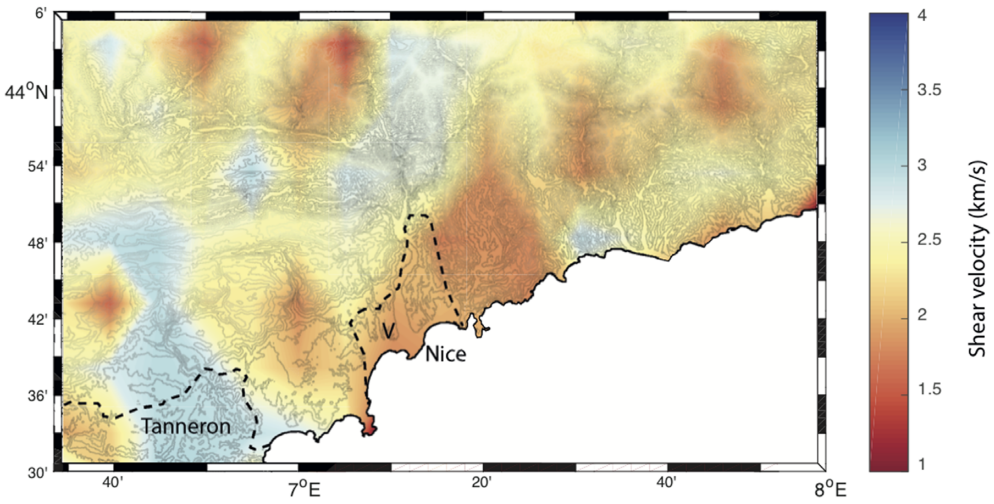

Figure 13. Depth slice through the 3-D final shear-velocity model, at 300 m, focused on the Alpes-Maritimes district. The dashed lines enclose the Tanneron massif and the Var-Paillon plaln.

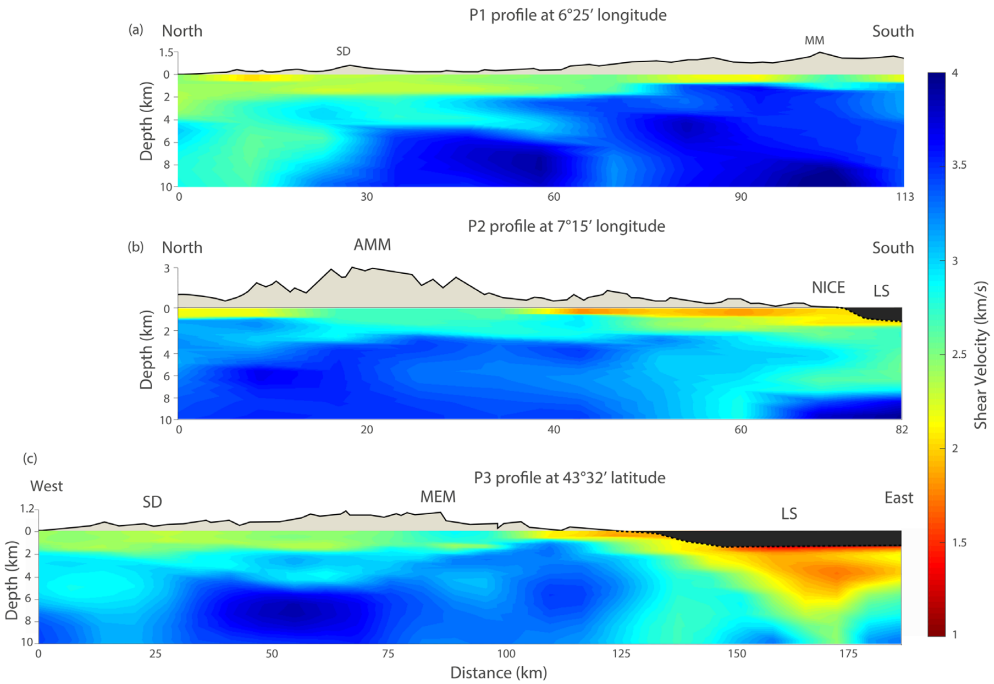

Figure 14. Vertical profiles P1, P2, P3 as mapped in Fig. 12, with same labels for toponyms and areas. Grey colour features the Ligurian Sea.

3 km s^{-1} which are consistent with velocities reported by Kästle *et al*. (2018) and Lu *et al*. (2018).

At depth ranging from 20 to 30 km depth, radial anisotropy was observed by Fry *et al*. (2010) in the orogen-parallel fast direction related to pre-alpine orogenic episode. However, at this regional scale and at shallower depth, no strong lateral variations of the radial anisotropy were identified from the comparison of Rayleigh and Love group velocity. Therefore, in this study we did not invert for radial anisotropy.

By looking both our Rayleigh and Love group velocity maps below 4 s (Figs 7 and 8), we can identify several areas featuring specific velocity anomalies. Two high-velocity zones around 3 km s^{-1}: (1) in the southwestern part from Toulon to the west of Nice, which corresponds, from west to east of the anomaly, to the succession of the Maures, Tanneron and Esterel (labelled MEM and T in Fig. 1) crystalline rock formations and (2) in the northeastern part of our covered zone, corresponding to the crystalline rock formations of Mercantour-Argentera massif (labelled AM in Fig. 1), the Dora-Maira massif (labelled DMM in Fig. 1) and the sedimentary cover of the internal alpine belt (labelled C in Fig. 1).

Between those two high-velocity anomalies, we can identify a low-velocity one of ∼2 km s^{-1} (Fig. 7) from the city of Nice to Digne-les-Bains, along the northwestern part of the covered zone. This area corresponds to the external zone of southwestern Alps called subalpine domain (labelled B in Fig. 1). We retrieve this velocity anomaly up to 5 s periods on the Rayleigh

group velocity maps (Fig. 7). The thick sedimentary cover in this area can explain this low-velocity anomaly. By looking the Love group velocity maps (Fig. 8), even if it's less obvious we can also identify this low velocity anomaly up to 3 s periods. However, a clearly visible low-velocity zone is retrieved centred on 44°N–6°E from 3 to 5 s periods which corresponds to the position of the Plio-Quaternary Durance-Valensole basin (labelled DVB in Fig. 1).

When focusing on Nice area, which has the highest density of stations, and for periods below 3 s, we can clearly identify a low velocity-zone, visible on both Rayleigh and Love wave group velocity maps between 1.5 and 4 s periods. At periods less than 2 s, much lower surface wave velocities are seen in this area. These areas consist of small sedimentary basins having sediments (alluvial, conglomerate and limestone aquifers) layers of several hundred metres like the Var valley (labelled V in Fig. 1) and the Paillon valley, located in the city of Nice (labelled N in Fig. 1). In the depth slices maps at 300 m (Fig. 12), we distinctly observe the same pattern of low velocity around this area. This distribution of velocity is also visible in the N–S profile P2 (Fig. 13b) down to 1 km depth from the coast to hinterland of Nice, an area known as Nice fold and thrust belt. Given the number of stations in this area, the resolution is maximum and allows us to locate superficial structures. At longer periods, between 5 and 9 s, the waves meet the crystalline substratum which is visible on the maps, as the velocity contrast with surrounding zones vanishes.

Finally, the lowest-velocity anomaly retrieved, visible throughout the whole periods, corresponds to the east Ligurian margin showing $\sim$1.5 km s^{-1} Scholte group-velocity wave. The $\sim$2.3 km s^{-1} velocity retrieved just opposite Toulon can be explained by the fact that ASEAF station is located at the bottom edge of the continental slope, so that the surface waves, at the period considered, are not very sensitive to the superficial part filled with water, unlike OBSs found in the eastern part. Overall, the quality of the OBSs' GF retrieved, especially at short periods, and the lack of station in this area make interpretation more difficult when looking at the east Ligurian margin. Many studies exist in the Ligurian Basin since some of the largest seismicity in the region is located there. Dessa *et al*. (2011) highlighted a first layer from the sea bottom (2.4 km) to 5 km depth with a *P*-wave velocity around 1.7 km s^{-1} down to 2 km s^{-1}, then a gradual increase in velocity from 2.8 km s^{-1} to 8 km depth. Using a *Vp*/*Vs* ratio of 1.7321, we find coherent low velocity anomalies in the vertical cross-sections and depth slices maps of the shear-wave velocity distribution compared to the ones observed by Dessa *et al*. (2011, Figs 11 and 13). Our observations highlight the presence of this low-velocity zone down to $\sim$6 km depth, which is linked to the presence of Salt and Evaporites from Plio-Quaternary deposits (Contrucci *et al*. 2001). In the eastern part, Lardeaux *et al*. (2006) identified *P*-wave velocities around 3.2 km s^{-1} at depth greater than 2 km, which is consistent with our shear-wave velocity model. Overall, the velocity anomaly retrieved below the 4 s group-velocity maps shows a good consistency with the major geological zones of the study area.

5 CONCLUSION

We used continuous three-component ambient noise recording obtained between 2011 and 2018 on 62 stations in the Southwestern Alps and the Ligurian margin. By correlating the noise records between every station pairs, we retrieved Rayleigh and Love wave GF and built 2-D group velocity maps and then a 3-D shear-velocity structure. The combined use of two depth inversions—first a Neighbourhood Algorithm for a coarse three layer models and then a linearized finite element approach—allowed us to observe distinctive velocity consistent with the surface geology. Most of the velocity variations are observed below 5 s. The 3-D shear velocity profiles highlight the thinning of the sedimentary complex above massifs, and conversely, its thickening in the subalpine domain, in the northwest of the area, and in the sedimentary basins located between the Esterel massif and the Dora-Maira massif on the Italian side. The low velocity zone identified under the Ligurian Sea down to $\sim$6 km depth is consistent with previous studies focusing on this part of the Ligurian Sea.

Given that most of the seismicity takes place in the Ligurian sea, a denser seismic network of broad-band sensors off shore of Nice could be useful to increase the area coverage at low period.

ACKNOWLEDGEMENTS

We are grateful for the constructive reviews provided by Dr Matthew Haney and an anonymous reviewer. The authors acknowledge the POSA group for providing funding and data. The authors acknowledge the Alparray group work E. Bertrand from Cerema for providing CASSAT and SISVAR data. We thank Mr and Mrs Metris for providing a quiet place to install one of the temporary station.

REFERENCES

AlpArray Seismic Network (AASN) temporary component, 2015. AlpArray Working Group. Other/Seismic Network. doi:10.12686/alparray/z3_2015.

Barmin, M., Ritzwoller, M. & Levshin, A., 2001. A fast and reliable method for surface wave tomography, *Pure appl. Geophys.,* **158**(8), 1351–1375.

Bensen, G.D., Ritzwoller, M.H., Barmin, M.P., Levshin, A.L., Lin, F., Moschetti, M.P., Shapiro, N.M. & Yang, Y., 2007. Processing seismic ambient noise data to obtain reliable broad-band surface wave dispersion measurements, *Geophys. J. Int.,* **169,** 1239–1260.

Béthoux, N., Fréchet, J., Guyoton, F., Thouvenot, F., Cattaneo, M., Eva, C., Nicolas, M. & Granet, M., 1992. A closing Ligurian Sea?, *Pure appl. Geophys.,* **139**(2), 179–194.

Béthoux, N., Tric, E., Chery, J. & Beslier, M.-O., 2008. Why is the Ligurian basin (Mediterranean Sea) seismogenic? Thermomechanical modeling of a reactivated passive margin, *Tectonics,* **27**(5).

Bigot-Cormier, F., Poupeau, G. & Sosson, M., 2000. Dénudations différentielles du massif externe alpin de l'Argenetra (Sud-Est de la France) révélée par thermochronologie traces de fission (apatites, zircons), *Comptes Rendus de l'Académie des Sciences de Paris,* **330,** 363–370.

Chamoot-Rooke, N., Gaulier, J.M. & Jestin, F., 1999. Constraints on Moho depth and crustal thickness in the Liguro–Provençal basin from 3D gravity inversion: geodynamic implications, in *In the Mediterranean-Basins: Tertiary Extension within the Alpine Orogen,* Vol. **156,** pp. 37–62, eds Durand, B. *et al.*, Geological Society of London Special Publication.

Contrucci, I., Nercessian, A., Béthoux, N., Mauffret, A. & Pascal, G., 2001. A Ligurian (Western Mediterranean Sea) geophysical transect revisited, *Geophys. J. Int.,* **146**(1), 74–97.

Dercourt, J. *et al.*, 1986. Geological evolution of the Tethyan belts from Atlantic to Pamirs since the Lias, *Tectonophysics,* **123,** 241–315.

Dessa, J.X. *et al.*, 2011. The GROSMarin experiment: three-dimensional crustal structure of the North Ligurian margin from refraction tomography and preliminary analysis of microseismic measurements, *Bulletin de la Société Géologique de France,* **182**(4), 305–321.

Dewey, J., Helman, M., Turco, E., Hutton, D. & Knott, S., 1989. Kinematics of the western Mediterranean, in *Alpine Tectonics,* Vol. **45,** pp. 265–283, eds Coward, M., Dietrich, D. & Parks, G.G., Geological Society of London Special Publication.

Faccenna, C., Mattei, M., Funicello, R. & Jolivet, L., 1997. Styles of back-arc extension in the Central Mediterranean, *Terra Nova,* **9,** 126–130.

Fry, N., 1989. Southwestward thrusting and tectonics of the western Alps, in *Alpine Tectonics,* Vol. **45,** pp. 83–109, eds Coward, M., Dietrich, D. & Park, R.G., Geolological Society of London Special Publication.

Fry, B., Deschamps, F., Kissling, E., Stehly, L. & Giardini, D., 2010. Layered azimuthal anisotropy of Rayleigh wave phase velocities in the European Alpine lithosphere inferred from ambient noise, *Earth planet. Sci. Lett.,* **297,** 95–102.

Gattacceca, J., Deino, A., Rizzo, R., Jones, D.S., Henry, B., Beaudoin, B. & Valeboin, F., 2007. Miocene rotation of Sardinia: new paleomagnetic and geochronological constraints and geodynamic implications, *Earth planet. Sci. Lett.,* **258,** 359–377.

Giannopoulos, D. *et al.*, 2017. Ambient noise tomography of the western Corinth Rift, Greece, *Geophys. J. Int.,* **211,** 284–299.

Hable, S., Sigloch, K., Stutzmann, E., Kiselev, S. & Barruol, G., 2019. Tomography of crust and lithosphere in the western Indian Ocean from noise cross-correlations of land and ocean bottom seismometers, *Geophys. J. Int.,* **219**(2), 924–944.

Haney, M.M. & Tsai, V.C., 2017. Perturbational and nonperturbational inversion of Rayleigh-wave velocities, *Geophysics,* **82**(3), F15–F28.

Hetenyi, G. *et al.*, 2018. The AlpArray seismic network: a large-scale European experiment to image the Alpine orogen, *Surv. Geophys.,* **39,** 1009–1033.

Ioualalen, M., Larroque, C., Scotti, O. & Daubord, C., 2014. The tsunami coastal distribution and hazard along the French–Italian Riviera, *Pure appl. Geophys.* **171,** 1423–1443.

INGV Seismological Data Centre, 1997. Rete Sismica Nazionale (RSN). Istituto Nazionale di Geofisica e Vulcanologia (INGV), Italy. http://doi.org/10.13127/SD/X0FXnH7QfY.

Jolivet, L. *et al.*, 2008. Subduction, convergence et extension arrière-arc en Méditerranée, *Bull. Soc. Geol. Fr.,* **179**(6), 525–550.

Jourdon, A., Rolland, Y., Petit, C. & Bellahsen, N., 2014. Style of Alpine tectonic deformation in the Castellane fold-and-thrust belt (SW Alps, France): Insights from balanced cross-sections, *Tectonophysics,* **633,** 143–155.

Kastle, E.D., El-Sharkawy, A., Boschi, L., Meier, T., Rosenberg, C., Bellahsen, N. & Weidle, C., 2018. Surface wave tomography of the Alps using ambient-noise and earthquake phase velocity measurements, *J. geophys. Res.,* **123,** 1770–1792.

Köhler, A., Weidle, C. & Maupin, V.J., 2012. On the effect of topography on surface wave propagation in the ambient noise frequency range, *J. Seismol.,* **16,** 221.

Lardeaux, J.M., Schwartz, S., Tricart, P., Paul, A., Guillot, S., Béthoux, N. & Masson, F., 2006. A crustal-scale cross-section of the south-western Alps combining geophysical and geological imagery, *Terra Nova,* **18,** 412–422.

Larroque, C. *et al.*, 2001. Active deformation at the junction between southern French Alps and Ligurian basin, *Netherlands Journal of Geosciences/Geologie en Mijnbouw,* **80**(3–4), 255–272.

Larroque, C., Delouis, B., Godel, B. & Nocquet, J.-M., 2009. Active deformation at the southwestern Alps–Ligurian basin junction (France–Italy boundary): evidence for recent change from compression to extension in the Argentera Massif, *Tectonophysics,* **467**. 22–34.

Larroque, C., Oona, S. & Mansour, I., 2012. Reappraisal of the 1887 Ligurian earthquake (western Mediterranean) from macroseismicity, active tectonics and tsunami modelling, *Geophys. J. Int.,* **190**(1), 87–104.

Laurent, O., Stéphan, J.F. & Popoff, M., 2000. Modalités de la structuration miocène de la branche sud de l'arc de Castellane (chaînes subalpines méridionales), *Géologie de la France,* **3,** 33–65.

Levshin, A., Yanovskaya, T., Lander, A., Bukchin, B., Barmin, M., Ratnikova, L. & Its, E., 1989. Recording, identification, and measurement of surface wave parameters, in *Seismic Surface Waves in a Laterally Inhomogeneous Earth,* ed. Keilis-Borok, V.I., pp. 131–182, Kluwer.

Lin, F.C., Moschetti, M.P. & Ritzwoller, M.H., 2008. Surface wave tomography of the western United States from ambient seismic noise: Rayleigh and Love wave phase velocity maps, *Geophys. J. Int.,* **173,** 281–298.

Lu, Y., Stehly, L. & Paul, A. AlpArray Working Group, 2018. High-resolution surface wave tomography of the European crust and uppermost mantle from ambient seismic noise, *Geophys. J. Int.,* **214**(2), 1136–1150.

Malinverno, A. & Ryan, W.B.F., 1986. Extension in the Tyrrhenian Sea and shortening in the Apennines as a result of arc migration driven by sinking of the lithosphere, *Tectonics,* **5,** 227–245.

Masson, F., Verdun, J., Bayer, R. & Debeglia, N., 1999. Une nouvelle carte gravimétrique des Alpes occidentales et ses conséquences structurales et tectoniques, *Comptes Rendus de l'Académie des Sciences de Paris,* **329,** 865–871.

Molinari, I., Verbeke, J., Boschi, L., Kissling, E. & Morelli, A., 2015. Italian and Alpine three-dimensional crustal structure imaged by ambient-noise surface-wave dispersion, *Geochem. Geophys. Geosyst.,* **16**(12), 4405–4421.

Mordret, A., Landès, M., Shapiro, N.M., Singh, S., Roux, P. & Barkved, O., 2013. Near-surface study at the Valhall oil field from ambient noise surface wave tomography, *Geophys. J. Int.,* **193**(3), 1627–1643.

Mordret, A., Landès, M., Shapiro, N., Singh, S. & Roux, P., 2014. Ambient noise surface wave tomography to determine the shallow shear velocity structure at Valhall: depth inversion with a Neighbourhood Algorithm, *Geophys. J. Int.,* **198**(3), 1514–1525.

Mordret, A., Rivet, D., Landès, M. & Shapiro, N.M., 2015. 3-D shear velocity anisotropic model of Piton de la Fournaise volcano (la Réunion island) from ambient seismic noise, *J. geophys. Res.,* **120**(1), 406–427.

Nocquet, J.-M., 2012. Present-day kinematics of the Mediterranean: a comprehensive overview of GPS results, *Tectonophysics*. **579**. 220–242.

Nunn, C. *et al.*, 2014b. Imaging the lithosphere beneath NE Tibet: Teleseismic P and S body wave tomography incorporating surface wave starting models, *Geophys. J. Int.,* **196**(3), 1724–1741.

Rawlinson, N. & Sambridge, M., 2004. Wavefront evolution in strongly heterogeneous layered media using the fast marching method, *Geophys. J. Int.,* **156**(3), 631–647.

Réhault, J.P., Boillot, G. & Mauffret, A., 1984. The western Mediterranean basin geological evolution, *Mar. Geol.,* **55,** 447–477.

RESIF-RLBP French Broad-band network, 1995. RESIF-RAP strong motion network and other seismic stations in metropolitan France. RESIF - Réseau sismologique & géodésique français. http://doi.org/10.15778/RESIF.FR.

Riccou, L.E. & Siddans, A., 1986. Collision tectonics in the western Alps, in *Collision Tectonics,* Vol. **19,** pp. 229–244, eds Coward, M. & Ries, A.C., Geolological Society of London Special Publication.

Rollet, N., Déverchère, J., Beslier, M.O., Guennoc, P., Réhault, J.P., Sosson, M. & Truffert, C., 2002. Back arc extension, tectonic inheritance and volcanism in the Ligurian sea Western Mediterranean, *Tectonics,* **21**(3), 6-1–6-23.

Sanchez, G., Rolland, Y., Corsini, M., Jolivet, M., Brichaud, S. & Carter, A., 2011. Exhumation controlled by transcurrent tectonics: the Argentera-Mercantour massif (SW Alps), *Terra Nova,* **23**(2), 116–126.

Sambridge, M., 1999a. Geophysical inversion with a neighborhood algorithm – I. Searching a parameter space, *Geophys. J. Int.,* **138**(2), 479–494.

Sambridge, M., 1999b. Geophysical inversion with a Neighbourhood Algorithm – II. Appraising the ensemble, *Geophys. J. Int.,* **138,** 727–746.

Schreiber, D., Lardeaux, J.M., Martelet, G., Courriou, G. & Guillen, A., 2010. 3-D modelling of Alpine Mohos in Southwestern Alps, *Geophys. J. Int.,* **180,** 961–975.

Séranne, M., 1999. The Gulf of Lions continental margin (NW Mediterranean) revisited by IBS: an overview, in *On the Mediterranean Basins: Tertiary within Alpine Orogen,* Vol. **156,** pp. 15–36, eds Durand, B., Jolivet, L., Horvath, F. & Séranne, M., Geological Society of London, Special Publication.

Shom, 2015. MNT Bathymétrique de façade du Golfe du Lion - Côte d'Azur (Projet Homonim). http://dx.doi.org/10.17183/MNT_MED100m_GDL_CA_HOMONIM_WGS84.

Stehly, L., Fry, B., Campillo, M., Shapiro, N.M., Guilbert, J., Boschi, L. & Giardini, D., 2009. Tomography of the Alpine region from observations of seismic ambient noise, *Geophys. J. Int.,* **178,** 338–350.

Schippkus, S., Zigone, D. & Bokelmann, G. the AlpArray Working Group, 2018. Ambient-noise tomography of the wider Vienna Basin region, *Geophys. J. Int.,* **215,** 102–117.

Thouvenot, F., Paul, A., Fréchet, J., Béthoux, N., Jenatton, L. & Guiguet, R., 2007. Are there really superposed Mohos in the south-western Alps? New seismic data from fan-profiling reflections, *Geophys. J. Int.,* **170,** 1180–1194.

Tricart, P., 1984. From passive margin to continental collision: a tectonic scenario for the western Alps, *Am. J. Sci.,* **284,** 97–120.

Verbeke, J., Boschi, L., Stehly, L., Kissling, E. & Michelini, A., 2012. High-resolution Rayleigh-wave velocity maps of central Europe from a dense ambient-noise data set, *Geophys. J. Int.,* **188**(3), 1173–1187.

Westphal, M., Orsini, J. & Vellutini, P., 1976. Le microcontinent corso-sarde, sa position initiale, données paléomagnétiques et raccords géologiques, *Tectonophysics,* **30,** 41–57.

Yao, H., Gouedard, P., Collins, J.A., McGuire, J.J. & van der Hilst, R.D., 2011. Structure of young East Pacific Rise lithosphere from ambient noise correlation analysis of fundamental- and higher-mode Scholte-Rayleigh waves, *C.R. Geosci.,* **343**(8-9), 571–583.